Numerical simulation of flow through tube bundles in in-line square and general staggered arrangements

Behzad Ghadiri Dehkordi and Hamed Houri Jafari

*Department of Mechanical Engineering, Tarbiat Modares University,
Tehran, Iran*

Abstract

Purpose – The purpose of this paper is to outline more computational schemes which provide a low computational cost approach to analyze flow characteristics through tube bundles. Flow through tube bundles has been numerically simulated by means of an alternative approach so as to assess flow behavior and its characteristics.

Design/methodology/approach – A Cartesian-staggered grid based finite-volume solver has been implemented. Furthermore, the ghost-cell method in conjunction with Great-Source-Term technique has been employed in order to directly enforce no-slip condition on the tubes boundaries. Before giving a solution for flow field through tube bundles, the accuracy of the solver is validated by simulation of flow in the cavity and also over a single circular cylinder. The results are completely compatible with the experiments reported in the literature.

Findings – Eventually, the flow through two types of tube bundles in in-line square and general staggered arrangements in Re = 100 are simulated and analyzed. For these tube bundles that are being studied, the maximum drag and lift coefficients and maximum gap velocities have been numerically obtained. The same simulations have been also performed for the cases where the tube bundles are confined by two lateral walls.

Practical implications – These configurations are frequently used in heat exchangers, steam boilers, nuclear reactors, and many mechanical structures.

Originality/value – The adapted method is firstly implemented to simulate flow through tube bundles and the analyzed simulations have not previously been presented by other researches.

Keywords Finite volume methods, Simulation, Flow, Numerical analysis

Paper type Research paper

1. Introduction

Solution of flow field through tube bundles for recognition of flow behavior is a matter of great importance in designing heat exchangers, nuclear reactors, and many industrial types of equipment. Tube bundles are known as very complex geometries for numerical investigations. The conventional structured-grid and new unstructured-grid approaches for simulating flow through tube bundles or other complex geometries are boundary-fitted. In these methods great simplicity of the enforcement of boundary conditions will be achieved. But transformation of the governing equations to the mesh coordinate system results in complexity of these methods (Ye *et al.*, 1999). Cartesian grid method does not have these problems but the governing equations are discretized on a grid which does not conform to the boundaries of the bluff bodies. The Cartesian grid method greatly simplifies the grid generation and also retains the relative simplicity of the governing equations. In addition, this method also has a significant advantage over the conventional boundary-fitted approach in simulating flows with moving boundaries (Shyy *et al.*, 1996; Ye *et al.*, 1999). Consequently, Cartesian grid methods have been used extensively for Euler flows (Almgren *et al.*, 1997; Pember *et al.*,

1995; Quirk, 1994; Bayyuk *et al.*, 1993) whereas applications to viscous flows were rare (Shyy *et al.*, 1996; Udaykumar *et al.*, 1996, 1997; Ye *et al.*, 1999).

Ye *et al.* (1999) proposed a method based on the Cartesian grid for simulating two-dimensional unsteady, viscous, incompressible flows over complex geometries. In this method, a control volume near the immersed boundary is re-formed into a body-fitted trapezoidal shape by discarding the solid part of the cell and adding the neighboring cells. This will lead to the different discretization for the reshaped cells yet add to the difficulty of the method. This method has been called "cut-cell" and is applicable in finite-volume method. They have simulated flow past a random array of 95 cylinders in Re = 24 in order to show the ability of the method in simulation of complex geometries. Another method that is developed for enforcement of boundary conditions on immersed boundaries in finite-volume method and Cartesian grid is called "ghost-cell" which is easier than the cut-cell method (Tseng and Ferziger, 2003). It should be pointed out that this method will not lead to a different discretization.

Cartesian grid based methods are also implemented to solve flow fields through tube bundles using penalization method. The penalization method was proposed for viscous flows by penalizing the momentum equations. Its main idea is to model solid obstacles as porous media with porosity, and viscous permeability approaching zero. Liu and Vasilyev (2007) have used penalization technique to simulate compressible flows through porous media based on a physically sound mathematical model. The penalization method is also used by other researchers (Kevlahan and Wadsley, 2005; Schneider and Farge, 2005) to solve the flow field and simulate the transient flow behavior in tube bundles as very complex geometries.

As it can be seen in reviewed papers, with regards to this fact that tube bundles are a kind of complex geometries, different numerical approaches could be chosen for simulation of flow through them. Furthermore, it should be mentioned that, generally, numerical simulations of flow through tube bundles with the goal of flow behavior analysis are scarcely done (Zdravistch *et al.*, 1995; Schroder and Gelbe, 1999; Sweeney and Meskell, 2003; Longatte *et al.*, 2003; Schneider and Farge, 2005), vs wide experimental researches which provides comprehensive data base for analysis many related phenomena with fluid-structure interactions.

Zdravistch *et al.* (1995) have numerically predicted laminar and turbulent fluid flow and heat transfer around staggered and in-line tube banks using a cell-centered finite-volume algorithm. Their results were included streamlines, pressure coefficient distributions, temperature contours, local Nusselt number distributions, and average convective heat transfer coefficients and they have found that a relatively fine grid is required to be able to predict the surface heat transfer behavior accurately.

Schroder and Gelbe (1999) and Longatte *et al.* (2003) have carried out some investigations on the numerical identification of fluid-elastic effects affecting tube bundle motion in cross-flows. Longatte's methodology was based on an arbitrary Lagrange Euler (ALE) formulation for the fluid computation and Schroder and Gelbe used STAR-CD software to analyze fluid-elastic instability in array of cylinders.

Sweeney and Meskell (2003) used a technique based on a discrete vortex method similar to the cloud-in-cell approach which has been applied to flow problems for small numbers of cylinders. Their numerical simulation was carried out for the unsteady flow through a rigid normal triangular tube array with a pitch-to diameter of 1.6. They determined both the frequency of vortex shedding and the instantaneous flow structure in the Reynolds number of 2,200.

Schneider and Farge (2005), studied the time evolution of several flows in arrays of cylinders, squares, and double-cruciform shaped tubes at a Reynolds number of 200 and pitch ratio of $P/D = 2$. Their numerical scheme is either based on adaptive wavelet or Fourier pseudo-spectral space discretization with adaptive time stepping. A volume penalization method has been used to impose no-slip boundary conditions on the tubes.

As it is evident, numerical studies on tube bundles are not extensively done and it seems necessary to outline more computational schemes which provide a low computational cost approach to analyze flow characteristics through tube bundles.

In this article, we have employed the finite-volume method and the ghost-cell technique to solve flow field through tube bundles with circular cylinders. Spatial discretization is based on a hybrid scheme on Cartesian-staggered grid while temporal discretization is in conformity with fully implicit practice. We also used a ghost-cell technique to enforce the no-slip condition on the embedded boundaries. The numerical procedure is based on the semi-implicit method for pressure-linked equations (SIMPLE) algorithm (Patankar and Spalding, 1972) in order to improve the convergence rate. A Great-Source-Term technique is employed for irregularity recognition and setting the flow field values on arbitrary grid point, instead of adding feedback-forcing to the Navier-stocks equations. A proper procedure is used to select the ghost-cells and then applying no-slip condition on the true physical boundary by a linear interpolation. Also, the process to enforce no-slip conditions on boundaries is simpler than such enforcements on typical cut-cell or penalization methods.

Regarding the adapted method, the flow field through two types of rigid tube bundles in in-line square and general staggered arrangements has been solved and analyzed in both unconfined and confined by lateral walls situations. Before solving the flow field through tube bundles, the accuracy of the solver is validated by simulation of flow in the cavity and also over a single circular cylinder.

The following section of the present article, therefore, outlines the governing equations, boundary conditions, and numerical formulation of the problem. Cavity flow simulation and validation of its results is presented in section 3 in order to ensure the accuracy of the method in such cases where there are no embedded boundaries in the domain. Section 4 describes the algorithm of selecting the ghost-cells and enforcement of no-slip condition on the true surface of embedded boundaries. This section also validates the approach for flow over a single circular cylinder and evaluates the accuracy in various Reynolds numbers by comparing the results with other experimental and numerical studies. In section 5, the results of flow field solution through tube bundles with circular cylinders is illustrated and analyzed. Finally, conclusions are drawn in section 6.

2. Problem formulation and numerical modeling
2.1 Governing equations
The governing equations on a two-dimensional, viscous, unsteady, and laminar flow field are continuity and momentum equations (Navier-Stocks equations), as:

$$\frac{\partial \rho}{\partial t} + \operatorname{div}(\rho \vec{u}) = 0, \tag{1}$$

$$\frac{\partial}{\partial t}(\rho u) + \operatorname{div}(\rho \vec{u} u) = \operatorname{div}(\mu \operatorname{grad} u) - \frac{\partial P}{\partial x} + \beta_x, \tag{2}$$

$$\frac{\partial}{\partial t}(\rho v) + \operatorname{div}(\rho \vec{u} v) = \operatorname{div}(\mu \operatorname{grad} v) - \frac{\partial P}{\partial y} + \beta_y, \tag{3}$$

where ρ is the fluid density, μ the fluid viscosity, $\vec{u}$ the velocity vector of flow field, P the pressure, and u and v are the velocity components in x and y directions, respectively. β_x and β_y are also body forces per unit volume.

In the present work, fluid has been assumed to be incompressible; therefore fluid density has been automatically retained as constant by the solver. In the performed numerical simulations there were no free surface in the numerical domain and the body forces has been consequently neglected ($\beta_x \approx 0, \beta_y \approx 0$).

2.2 Boundary conditions
Boundary conditions should be enforced on the inlet, the outlet, and the boundaries of the computational domain and also on interior region and surfaces of embedded boundaries. Dirichlet boundary condition has been generally used on the boundaries of the computational domain except for the outlet where a Neumann boundary condition has been employed. The boundary conditions in the inlet of the flow consist of $u = U$ and $v = 0$, where U is the free-stream velocity. Neumann boundary conditions at the outlet of computational domain include:

$$\frac{\partial P}{\partial x} = 0, \frac{\partial u}{\partial x} = 0 \text{ and } \frac{\partial v}{\partial x} = 0.$$

Enforcement of no-slip condition on the embedded boundaries is the main difficulty of the method which is described in sections 4.1 and 4.2. The values of the flow field variables have been arranged to be the solution at the embedded boundaries grid points by Great-Source-Term technique described in section 2.5.

2.3 Grid generation
We have used fixed Cartesian-staggered grid with non-uniform grid spacing. The grids in the region of the embedded boundaries are sufficiently finer in order to achieve reasonable accuracy. The velocity components are calculated for the points lying on the faces of the control volumes in the staggered grid and pressure is calculated for the main scalar grid points.

2.4 Discretization of governing equations
The governing equations have been discretized using the finite-volume method. The temporal discretization has been done in conformity with the fully implicit practice. For the spatial discretization, Hybrid scheme has been employed. Discretized equations including momentum equations, pressure and velocity correction equations are described in detail by Patankar (1980) and we avoid reiterating their presentation here. But it must be pointed out that the function $A(|P|)$ would appear in algebraic discretized equations where P is the Peclet number and function A can be selected in relation to the spatial discretization scheme. With regard to the Hybrid scheme of this article, the cited function is selected, for which:

$$A(|P|) = [[0, 1 - 0.5|P|]], \tag{4}$$

The function $[[,]]$ will select the maximum argument. S_C and S_P will also appear in discretized equations which are the components of linearized source term ($\overline{S} = S_c + S_p \phi_p$). In addition, pressure gradient is included in this source term. ϕ_p is

the independent variable evaluated in the pole point of grid and can stand for velocity components in momentum equations, or pressure correction in the continuity equation.

2.5 Method of irregularity recognition

Our computer program is written for Cartesian grid but can be improvized to perform an irregularly shaped calculation domain. This is done by rendering inactive cells or "blocking-off" some of the control volumes of the regular grid so that the remaining active control volumes form the desired irregular domain. The blocking-off operation consists of establishing known values of the relevant ϕ's in the inactive control volumes, which in the present work is performed by implementing Great-Source-Term techniques.

In this manner, any desired value of ϕ (e.g. interpolated values for u and v on the boundary the bluff bodies) can be arranged to be the solution at an internal grid point by setting S_C and S_P as follows:

$$S_C = 10^{30}\phi_{P,\text{desired}} \qquad (5)$$

$$S_P = -10^{30} \qquad (6)$$

where 10^{30} denotes a number large enough to make the other terms in the discretization equation negligible. Consequently,

$$S_C + S_P\phi_P \approx 0.0 \Rightarrow \phi_P = -\frac{S_C}{S_P} = -\frac{10^{30}\phi_{P,\text{desired}}}{-10^{30}} = \phi_{P,\text{desired}} \qquad (7)$$

2.6 Numerical solution algorithm

We used the SIMPLE procedure for calculation of the flow field. The SIMPLE algorithm (Patankar and Spalding, 1972) is based on a cyclic series of guess-and-correct operations to solve the discretized governing equations. First, the velocity components are computed using the momentum equations and a guessed pressure distribution. Then, the mass residual (b) is calculated and the pressure and velocity components are corrected in order to satisfy the continuity equation ($b \approx 0.0$).

2.7 Convergence criterion

Residuals are the main factors for setting the convergence criterion in the solver. The residuals consist of the sum of mass source (b) and the sum of residual source within the calculation domain for continuity and momentum equations in x and y directions, respectively. The value of these mentioned residual sources must be lower than the adjusted convergence criterion in order to stop the iterations in every time step. The value of convergence criterion has been safely set at 10^{-6} in the present work. It implies that all three residual sources must have values smaller than the convergence criterion.

3. The cavity flow

In order to validate the developed solver before adding any embedded boundary and in the case of fitted grids on the boundaries of computational domain, numerical simulations on the cavity flow have been preliminarily performed. The cavity flow is a

conventional problem in computational fluid dynamics with wide implementation in validation of numerical models. There are many analytical and numerical investigative data. In addition, the boundary condition of this flow is easy to apply. The computational domain of the problem is figured in Figure 1. D is the length of each side of the cavity and U is the flow velocity at the upper side. Based on these scales of the problem, the Reynolds number is defined as $\text{Re} = \rho U D / \mu$.

Simulations have been done on two different Reynolds numbers of 100 and 400. In these Reynolds numbers the flow regime in the cavity is laminar and steady. The cavity is filled with incompressible fluid with $\rho = 1000$ and $\mu = 0.001002$. The length scale of the cavity and velocity of upper side have been set at $D = 1$ and $U = 0.0001002$ to achieve Reynolds number of 100. For Reynolds number equal to 400, $U = 0.0004008$ has been adjusted.

The boundary conditions of lateral and bottom sides include zero values of velocity components ($u = 0, v = 0$) and the boundary conditions of upper side are $u = U$ and $v = 0$. Simulations performed on a uniform grid with 200 by 200 grid cells. And also the solver has been run in the steady state situation by setting the time step to a great value ($\Delta t = 10^{30}$) and the convergence criterion have been set at 10^{-6}.

Figure 2 shows the u- and v-velocity profiles in a section of the cavity which $x = D/2$ and $y = D/2$, respectively. These velocity profiles for two Reynolds numbers, $\text{Re} = 100$ and 400, are compared with Ghia *et al.* (1982). The results from the present work are shown in solid and dashed lines and the data points in symbols stand for Ghia's results. As it is evident the results are in good agreement.

For more comparison, the calculated streamlines of the flow field in the cavity, are compared with the numerical results of Hou and Zou (1995) which are shown in Figure 3. The streamlines are quite consistent in both $\text{Re} = 100$ and 400. In general, three vortices are formed in these Reynolds numbers; two smaller vortices in the bottom corners and one big vortex in the center of the cavity. The vortices in the corners of the cavity in $\text{Re} = 400$ are larger than the case of $\text{Re} = 100$. The ability to locate the center of the vortices has been also observed. When $\text{Re} = 100$, the current method estimates the center of the large vortex at (0.621, 0.742) compared to (0.6196, 0.7373) found with the Hou and Zou method. When $\text{Re} = 400$, the current method estimates the center of the large vortex at (0.572, 0.613) in comparison to (0.5608, 0.6078) from Hou and Zou.

It can be concluded that the numerical formulation and algorithms are correctly implemented and we can use them to solve more complicated flow fields.
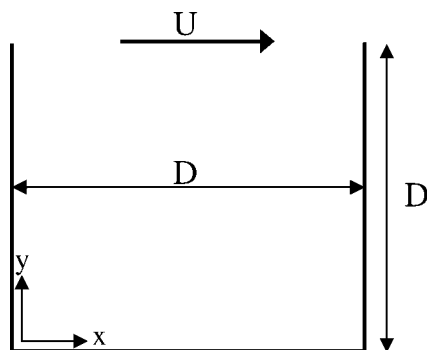

Figure 1.
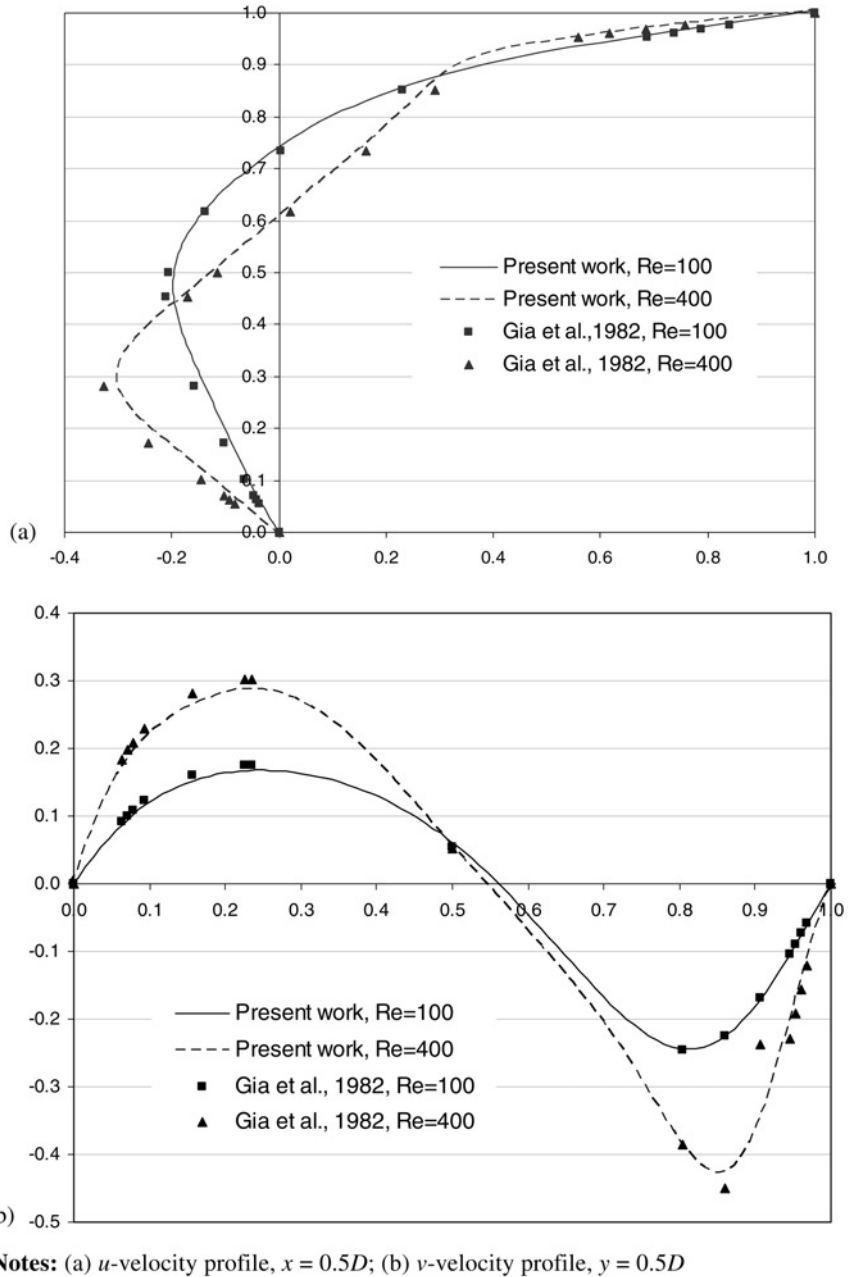Computational domain of
the cavity flow problem

Figure 2.
Comparison of velocity profiles along a line cut through the center of the cavity at Re = 100 and 400

Notes: (a) *u*-velocity profile, *x* = 0.5*D*; (b) *v*-velocity profile, *y* = 0.5*D*

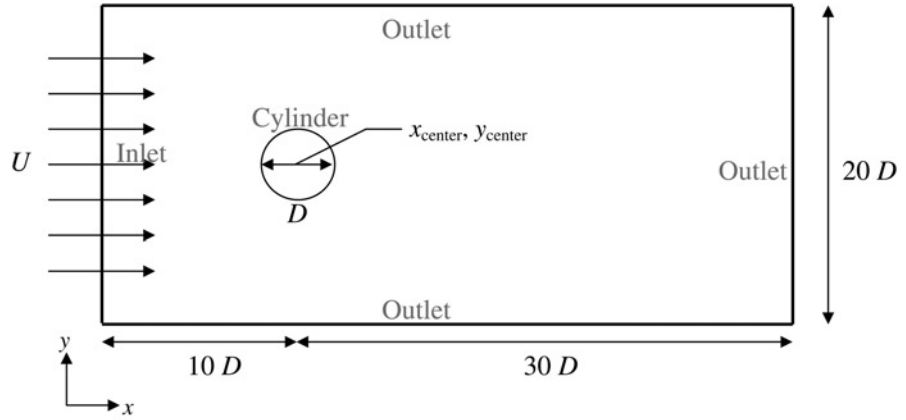## 4. Flow around a single circular cylinder

With regard to the target of the present article to simulate fluid flow in tube bundles with circular cross sections, the validation of the solver for the flow around a circular cylinder is a matter of great importance. There are also many numerical simulations to compare with our results.
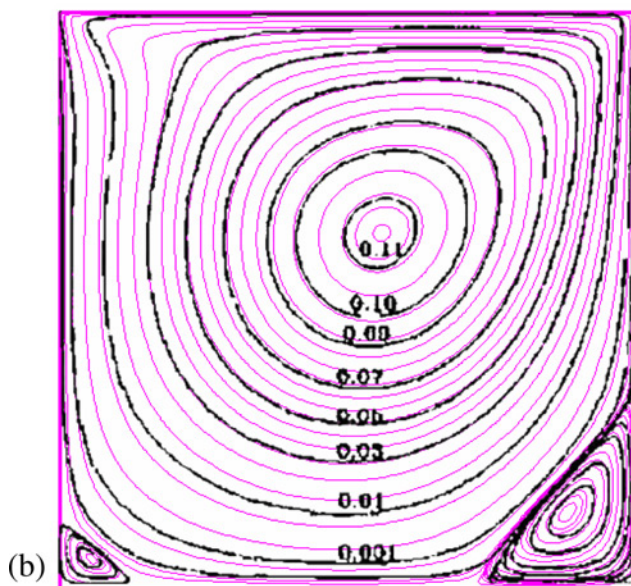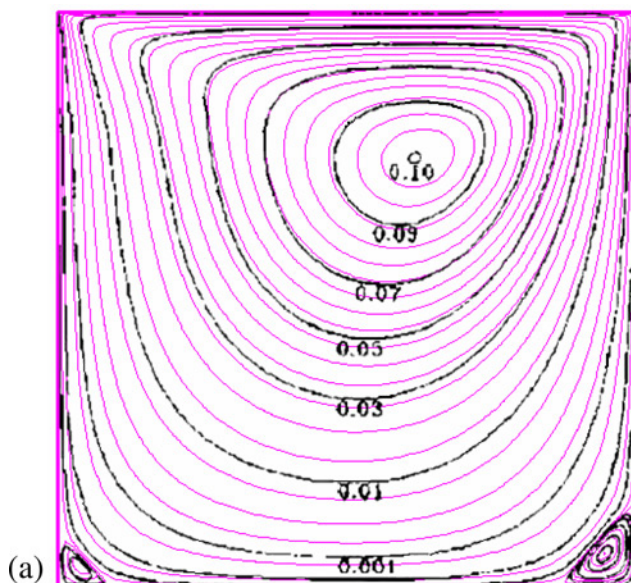
Figure 3.
Comparisons of
streamlines obtained in
the present work (in grey),
and those from Hou and
Zou (1995) (in black)

Notes: (a) Re = 100; (b) Re = 400

In the present simulation, a rectangular domain was used to simulate the flow around a stationary circular cylinder; see Figure 4. The domain had a length of 40*D* and a width of 20*D*, where *D* is the cylinder diameter. These dimensions were chosen in order to safely minimize the boundary effects on the flow development. Cylinder was placed inside the domain so that its center had coordinates $x = 10D$ and $y = 10D$. The

Note: Cylinder is not drawn to scale

boundary conditions were imposed in a way that the fluid flowed from left toward right
into the downstream of the domain. A Neumann boundary condition was used on the
lateral boundaries and uniform velocity profile U was specified at the domain entrance.

In order to compare the results, various parameters have been used as follows:

$$\text{Reynolds number: Re} = \frac{\rho UD}{\mu}, \tag{8}$$

$$\text{Drag coefficient: } C_D = \frac{F_D}{0.5\rho U^2 D}, \tag{9}$$

$$\text{Lift coefficient: } C_L = \frac{F_L}{0.5\rho U^2 D}, \tag{10}$$

$$\text{Pressure coefficient: } C_p = \frac{P}{0.5\rho U^2}, \tag{11}$$

$$\text{Strouhal number: } St = \frac{fD}{U}, \tag{12}$$

$$\text{Dimensionless time: } T = \frac{tU}{D}, \tag{13}$$

where F_D and F_L are the drag and lift forces (including pressure and friction drags and
lifts), respectively, P the pressure, f the vortex shedding frequency (if vortex shedding
exists) and t is the time.

In the whole state of the numerical simulation of the flow around circular cylinders
the flow assumed incompressible with $\rho = 1,000$ and $\mu = 0.001002$. Cylinder diameter
has been also taken as $D = 0.04$. Simulations have been performed in Re = 10, 20, 40,
80, 100, 150, and 300; to achieve the cited Reynolds numbers the free-stream velocities
have been taken as $U = 0.0002505$, 0.000501, 0.001002, 0.002004, 0.002505, 0.0037575,
and 0.007515, respectively. The reason for the selection of these Reynolds number is
to check a wide range of laminar flow regimes and also make comprehensive
comparisons with other numerical simulations. This can help us find out the accurate
range of the function of the solver.

The flow around a circular cylinder has evidently been the case with the embedded boundary. It must be reminded that in this case, some difficulties arise due to existing curved boundaries on Cartesian grids where the grid points are not coincided on the true surface of them. So before presenting the solution of above mentioned simulations, it is necessary to describe ghost-cells selection procedure and indication of the flow field values for these cells in order to satisfy the no-slip condition on the true surface of embedded boundaries. Cited procedures are described in next subsections (4.1 and 4.2). Investigation of grid-independency and validation of flow around a circular cylinder have been also done in sections 4.3 and 4.4, respectively.

4.1 Selection of cut- and ghost-cells
Since boundaries of circular cylinders have curvatures, the grid points of Cartesian grid both in staggered and scalar grid do not fit on the boundaries. Therefore enforcement of no-slip condition has some difficulties. If the embedded boundary had rectangular shape, this problem would not exist. The goal is to remedy the problem with minimum computational cost.

As it was previously mentioned, a solution is the cut-cell technique which will lead to different discretization for boundary cells and high computational expenses and complexity (Ye *et al.*, 1999). Another applicable technique in finite-volume solvers is the ghost-cell. In this technique, ghost-cell is a cell that has been cut by physical boundaries of obstacles and location of its flow field values (e.g. velocity components or pressure) lies in the interior region of the boundary. The cells which lie in the exterior region of the boundary are fluid cells. We must calculate the values of ghost-cells with the aid of interpolation and use of the exterior points in order to satisfy no-slip condition on the true surface of bluff body (Tseng and Ferziger, 2003).

Before the interpolation, the ghost-cells must be indicated. Regarding to the use of staggered grid in this work, location of velocity components and pressure is different for a cell where this point should be seriously considered. Firstly, the cells which are cut by the boundary are selected, as illustrated in Figure 5. Distance of four corners of all the grid cells from the center of cylinder location is calculated to select these cells. The cell is exterior if all these four distances are larger than cylinder diameter, the cell is interior if all these four distances are smaller than cylinder diameter, and finally cut-cells are selected if some distances are larger and others are smaller than the cylinder diameter. In Figure 5, the cut-cells are shown in gray and interior cells are hatched for main grid (not staggered). If the location of flow field values rest into the boundary (G1, G2, and G3 points) the cell is ghost and their value will be calculated by interpolation. If the location of flow field values rest out of the boundary (F1, F2, and F3 points) there is no need for any interpolation and its value will be calculated by solution of the flow field.

The abovementioned procedure is loyal for u and v staggered grids and has been identically repeated. Finally in Figure 5, locations of u and v which needs interpolation are shown by solid arrows and locations where values are calculated in the flow field are shown by hollow arrows. Interpolation procedure of ghost values is described as follows.

4.2 Enforcement of the no-slip condition
Setting to zero the values of velocity components for selected boundary cells in previous section (both ghost-cells and flow cells near boundary) is the simplest way to enforce no-slip condition. This practice will lead to correct solution when grid is infinitely refined. Thus, this method is really impossible due to the limited computational aspects. We did this practice with practical grid size (not infinite) where

Figure 5.
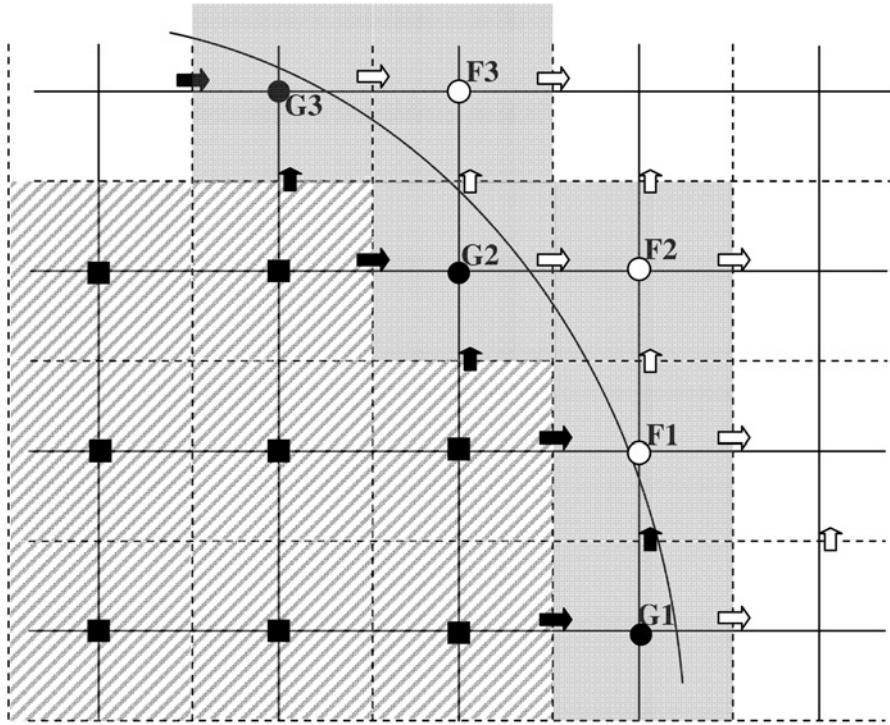Cells that are cut by
cylinder boundary and
calculation location of
flow field values for
main grid

Notes: ➡ Location of u-velocity in ghost-cell of u-staggered grid. ⬆ Location of v-velocity in ghost-cell of v-staggered grid. ● Location of pressure in main grid. ⇨ Location of u in flow field. ⇧ Location of v in flow field. ○ Location of pressure for a cell located in the flow field; cat-cells are in gray and internal cells are hatched

the method has yielded the jagged pressure distribution. The goal of ghost-cell technique is to prevent this jagged pressure distribution.

We used linear interpolation scheme proposed by Tseng and Ferziger (2003) in order to perform the ghost-cell method. They have shown that assumption of linear variation of the flow field values near the boundary have approximately the same accuracy with quadratic variation assumption. If ϕ stands for flow field variables (pressure and velocity components), then its variation near the boundary is as follows:

$$\phi = a + bx + cy, \tag{14}$$

where a, b, and c are the constant coefficients and x and y are the coordinates of ϕ's calculation place. Three points with known flow values are needed for calculation of constant coefficients and finally ϕ in the ghost-cell (ϕ_G). Two of the points mentioned and used in this work are as follows:

(1) A point on the real surface of cylinder that will be obtained from the cross point of cylinder boundary and a line between cylinder center and the ghost point location. Value of this point is the very boundary condition (e.g. $\phi = 0.0$ in the case of stationary cylinder).

(2) Two exterior points (F points) which are the nearest to the real boundary. Value
of ϕ in these two points are obtained from the flow field in previous iteration of
SIMPLE algorithm.

It should be pointed out that in the staggered-grid, the constant coefficients of equation
14 are quiet different for pressure and velocity components due to the different places
of calculation of the pressure and velocity components. Here, Great-Source-Term
technique is employed to set the interpolated values as the solution of ghost-cells.

4.3 Investigation of grid-independency

Four grid types with various sizes are studied in order to investigate grid-independency
of results. Grid-independency is proved in this section and shown that the results are not
sensitive to the grid size. The results of the study are shown in Table I. In this table,
pressure drag coefficient, fraction drag coefficient, total drag and angle of separation in
the flow around a single circular cylinder in Re = 40 are summarized for four grid sizes.
Grid sizes include: fine grid A, standard grid B, coarse grid C, and coarser grid D. In all
grid types, grids are finer in the region of cylinder in a manner that 20 through ten cells
lying along the cylinder diameter in fine grid through coarser grid, respectively; N_D in
Table I represents the number of cells lying within the cylinder.

It must be mentioned that the simulation is done in unsteady condition with time
step $\Delta t = 10^{-3}$. The simulation is continued to get stationary condition, regarding the
steady flow behavior in Reynolds 40.

As it is observed from Table I, results are fully independent from grid sizes. For
example, total drag coefficient for simulation type D is equal 1.436 while in simulation
type A is equal 1.52 that has reasonable 5.5 percent difference. Also, our study has shown
that the results have no significant difference for grids finer than grid type A. Hereinafter,
all presented results were obtained by grid type A with 200×200 cells (Figure 6).

Re = 40 Simulation	N_{cells}	N_D	Domain	$C_{D,p}$	$C_{D,s}$	C_D
A fine grid	180×200	20	$[20D \times 40D]$	1.010	0.510	1.520
B standard	140×160	16	$[20D \times 40D]$	0.998	0.509	1.507
C coarse grid	100×120	12	$[20D \times 40D]$	0.975	0.497	1.472
D coarser grid	80×100	10	$[20D \times 40D]$	0.967	0.469	1.436
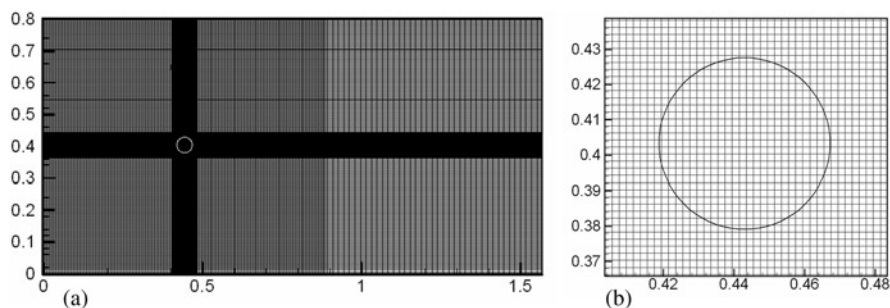
Notes: (a) Complete view of the domain and (b) zoom view of the refined region

4.4 Verification and analysis of the results

Results of the flow around single circular cylinders are verified and analyzed in this section using defined dimensionless parameters (equations 9-13). Figure 7 demonstrates the pressure distribution for Reynolds numbers of 40 and 100. Good agreement exists between present work and other studies.

Our simulations generally show that for Reynolds numbers equal to 10, 20, and 40, the flow field is fully symmetric and steady. Twin vortices are formed behind the cylinder that they are stationary. The vortices' length increases with the Reynolds number. In Reynolds numbers of 10, 20, and 40 the symmetry of the pressure field with respect to the x-axis explains the absence of lift due to these flows. Therefore, Lift coefficient is zero for these
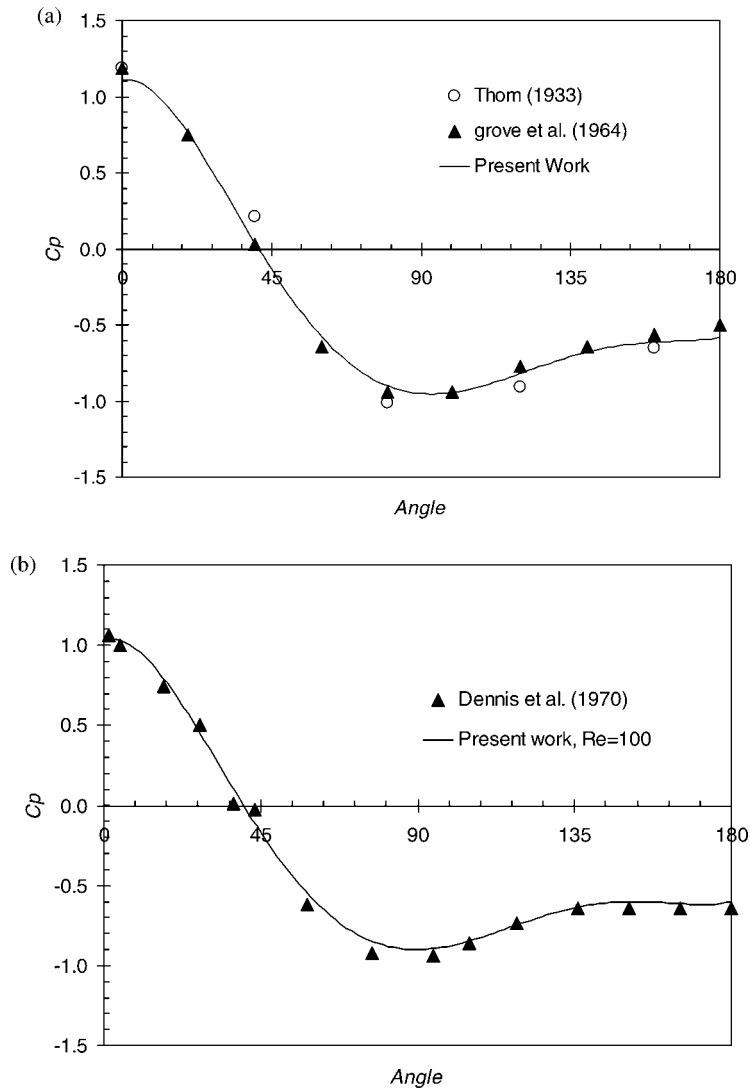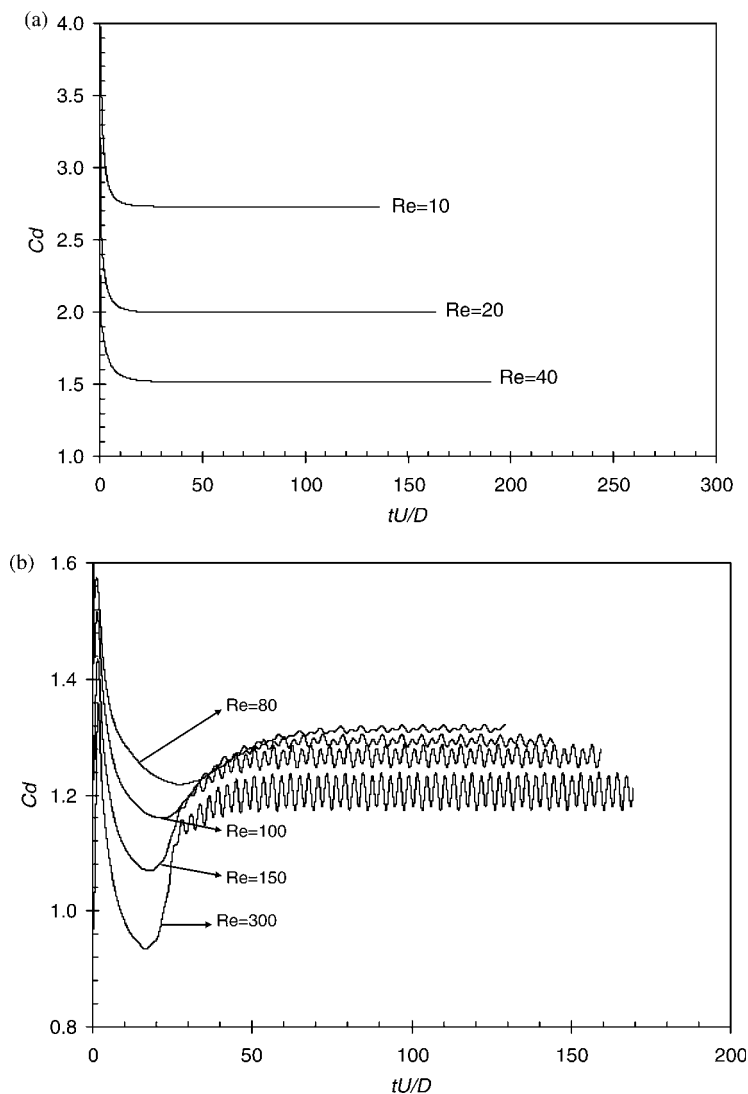

Figure 7.
Pressure distribution obtained by the present work in comparison with some experimental and numerical results in the literature

Notes: (a) Re = 40 and (b) Re = 100

Reynolds numbers. For Reynolds number 80 and above, Von karman street is formed behind the cylinder and flow field is unsteady and asymmetric. Thus, lift and drag coefficients oscillate due to the oscillation of separation point location. Moreover, the drag coefficient oscillates at twice the frequency of the lift coefficient.

In order to show variation patterns of drag coefficient, we have graphed the drag coefficient as a function of the dimensionless time for different values of the Reynolds number in Figure 8. Similar graphs are drawn by Lima E Silva *et al.* (2003) and our purpose was the comparison of our work with their results. In the mentioned reference case, an immersed boundary method based on finite differences has been developed.

Notes: (a) Re = 10, 20, 40, and 50 and (b) Re = 80, 100, 150, and 300

Figure 8.
Drag coefficients vs the
dimensionless time

Their Cartesian grid was uniformly generated with the size of 250×500. Grid point's number along the diameter was 17 while in present work grid size is 200×200 with 20 cells along the diameter. Total number of their mesh is 1,25,000 and total number of our mesh is 40,000 which is one-third of their mesh size. Drag coefficients drawn in Figure 8 are in good agreement with the same graphs presented by Lima E Silva *et al.* (2003). Only there is some differences in $Re = 300$ due to the three-dimensionality in this Reynolds number. As it can be observed in Figure 8, the amplitude and frequency of the drag coefficients increase as the Reynolds number increases. For $Re = 10$, 20, and 40, the drag coefficients are high at the beginning and asymptotically decay to 2.73, 1.99, 1.52, and 1.4, respectively, as shown in Figure 8(a).

Maximum amplitude of lift coefficients in $Re = 80$, 100, 150, and 300 are also calculated as 0.2, 0.29, 0.4, and 0.48, respectively. In these Reynolds numbers the frequency of oscillating lift is similar to the vortex shedding frequency. Strouhal number for these Reynolds numbers are 0.152, 0.163, 0.179, and 0.198, respectively, which for 80, 100, and 150 are in excellent agreement with literature (e.g. Williamson, 1996 and Roshko, 1955) and for Reynolds number of 300 there is weak agreement but it is consistent.

Comparison between the mean drag coefficients in different numerical and experimental investigations including present work are presented in Table II. As it is observed, the results for the drag coefficient are consistent with the results of other studies.

Finally, Figure 9 illustrates the corresponding vorticity field for Reynolds numbers of 20, 40, 80, 100, 150, and 300. The symmetrical flow for Reynolds 20 and 40 can be visualized in this figure. In these Reynolds numbers shear layers in both upper and lower sides of cylinders have the greatest amount of vorticity. For Reynolds number 80 and more than that, vortices shed from the cylinder. The intensity of the vortices is dramatically decayed shortly after generation (see Figure 9(c)-(f)). These intensification characteristics show that the vortices are continuously receiving energy from the shear flow and losing energy by viscous dissipation. The shear flow at the back of the cylinder is not well established and the vortices lose their energy very quickly by viscous dissipation. Further downstream, the shear flow becomes intense and organized and the vortices are able to receive more energy than they lose. Subsequently, the vortices enter a region where the shear flow is not as intense and they start to lose more energy than they receive. By increasing the Reynolds number (80-300), the vortices become stronger and Von Karman Street vanishes more gradually.

Regarding the performed verification of the flow around a single cylinder in this section, the present work has acceptable accuracy in the two-dimensional limits and in the absence of three-dimensionality. In the next section the flow through tube bundles are investigated and analyzed by adding more embedded cylinders in the computational domain.

5. Flow through tube bundles
We have verified the accuracy of the method of this paper for some typical flows. The main objective of the current work however has been to simulate flows through tube bundles. Tube bundles have complex geometry with many more cylinders than single cylinder geometry. Arrangement of cylinders is important and affects behavior of the flow through the tube bundle. Typical arrangements for heat exchangers are considered in the present work in $Re = 100$. Flow has no three-dimensionality effect for Reynolds numbers below 1,000 (Kevlahan and Wadsley, 2005). Thus we can safely use the present solver. Henceforth, the flow field in the tube bundle with in-line square arrangement and 36 cylinders and then in general staggered arrangement with 61 cylinders are numerically simulated. The simulations have been also done for confined

Reference	Re	C_D	Comments
Present work	10	2.73	Cartesian-staggered grid, Finite-volume method
	20	2.00	
	40	1.52	
	80	1.31	
	100	1.29	
	150	1.27	
	300	1.21	
Lima E. Silva *et al.* (2003)	10	2.81	Cartesian grid, Finite differences method, Immersed
	20	2.04	boundary method
	40	1.54	
	80	1.40	
	100	1.39	
	150	1.37	
	300	1.27	
Park *et al.* (1998)	10	2.78	(C-grid/domain) polar upstream and rectangular
	20	2.01	downstream, Finite differences method
	40	1.51	
	80	1.35	
	100	1.33	
	300	1.37	
Kravchenko *et al.* (1999)	40	1.52	Polar zonal grid, Finite difference method
	100	1.31	
Dennis and Chang (1970)	20	2.05	Polar grid, Finite difference method, Steady state
	40	1.52	solution
Ye *et al.* (1999)	20	2.03	Cartesian cell-centered collocated grid, Finite-Volume
	40	1.52	method, Cut-cell technique
	80	1.37	
	300	1.38	
Tseng and Ferziger (2003)	40	1.53	Cartesian cell-centered collocated grid, Finite-Volume
	100	1.42	method, Ghost-cell technique
Tritton (1959)	20	2.22	Experimental
	40	1.48	
	80	1.29	
	100	1.25	
Henderson (1995)	100	1.30	Experimental

Table II.
Comparison of the mean
drag coefficient obtained
by the present work
with some experimental
data and numerical
results

tube bundle cases where the flow domain is bounded by two lateral walls. The results of these for configuration are summarized in Table III and analyzed as follows. Fluid specification, time step, convergence criterion, and other situation are similarly set as the flow around a single circular cylinder problem of the previous section. Note that flows are impulsively started by imposing free-stream velocity.

5.1 Tube bundle in in-line square arrangement
5.1.1 Unconfined case. In this section, we presented the computed results of the flow field through an unconfined tube bundle with in-line square arrangement. These configurations are frequently used for cross-flow heat exchangers and static mixers.
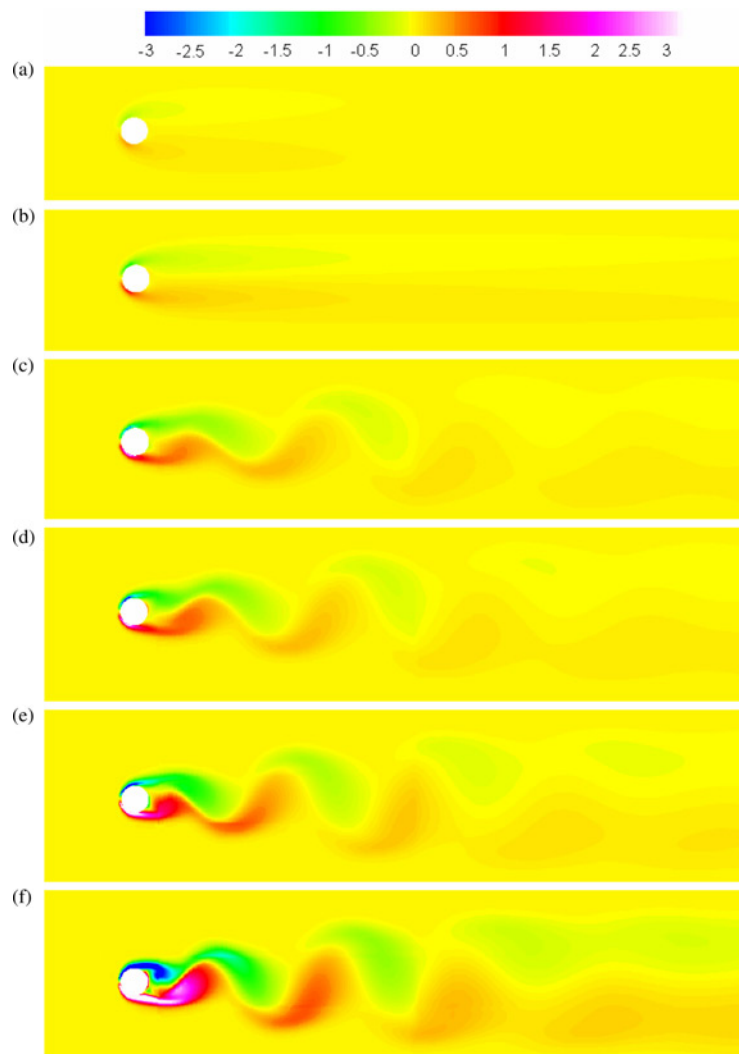
Figure 9.
Vorticity field of flow
around a circular cylinder

Notes: (a) Re = 20, (b) Re = 40, (c) Re = 80, (d) Re = 100, (e) Re = 150 and
(f) Re = 300

Tube bundle arrangement	In-line square with 36 cylinders		General staggered with 61 cylinders	
	Unconfined	Confined	Unconfined	Confined
Maximum drag coefficient	1.06	1.97	0.75	2.85
Average drag coefficient	0.118	0.214	0.065	0.327
Maximum lift coefficient	0.11	0	0.46	0.74
Average lift coefficient	0	0	0	0
Maximum gap velocity	1.74U	2.53U	1.87U	2.49U

Table III.
The results obtained for
the flow through tube
bundles in Re = 100

In addition of Table III, for analysis of the results, we have shown flow visualizations of instantaneous vorticity fields, pressure contours, and streamlines.

In Figure 10, we sketch the flow configuration for bundles of tubes with in-line arrangement and free-stream velocity of U. The geometry is characterized by the pitch-to-diameter ratio P/D, where D denotes the tube diameter and P the bundle pitch. In industrial applications, the ratio is typically between 1.3 and 2. Reynolds number is defined based on the tube's diameter and the free-stream velocity is equal to 100. In the present simulations $D = 0.04$ and $P/D = 2$ are taken. The number of cylinders in the tube bundle is 36 and all of them are stationary and inflexible and are imposed to viscous, incompressible, and unsteady cross-flow. Mesh size is 360×390 and finer in the region of the tube bundle with 20 lying cells within every cylinder.

In Figures 11-13 we show snapshot of the vorticity field, pressure contours, and streamlines, respectively, at $tU/D = 20$, $\mathrm{Re} = 100$. General flow pattern in Figure 11, is in good agreement with the results of Schneider and Farge (2005) simulation in $\mathrm{Re} = 200$. The highest vorticity is seen on the cylinders of middle rows. Also, the flow behind the tube bundle is rotational. Since there is no solid in regions far from tube bundle, vorticity is equal to zero in those regions. The symmetric pattern of flow
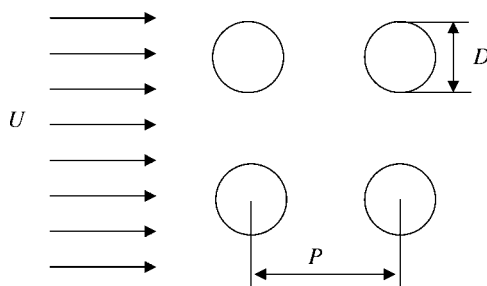

Figure 10.
Schematic of flow through a tube bundle with tube pitch P, tube diameter D, and pitch-to-diameter ratio P/D
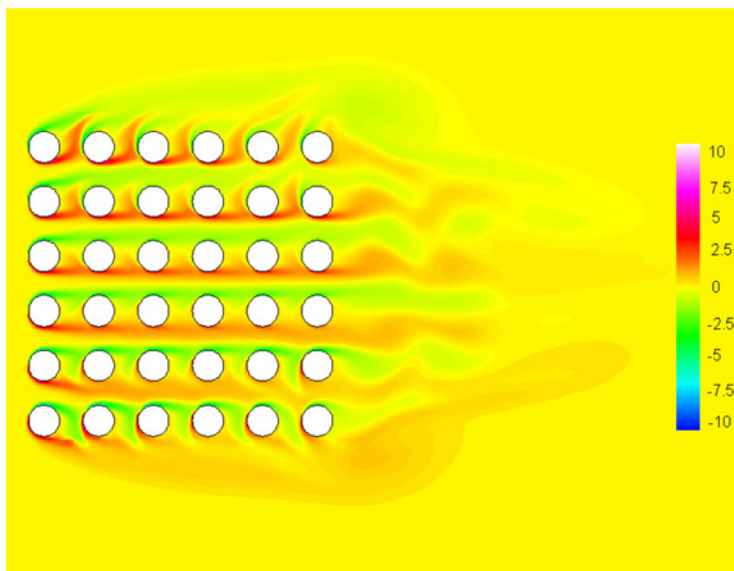

Figure 11.
Vorticity field computed for tube bundle in in-line square arrangement with 36 cylinders at $tU/D = 20$, $\mathrm{Re} = 100$, and $P/D = 2$

Figure 12.
Pressure contours
obtained for tube bundle
in in-line square
arrangement with 36
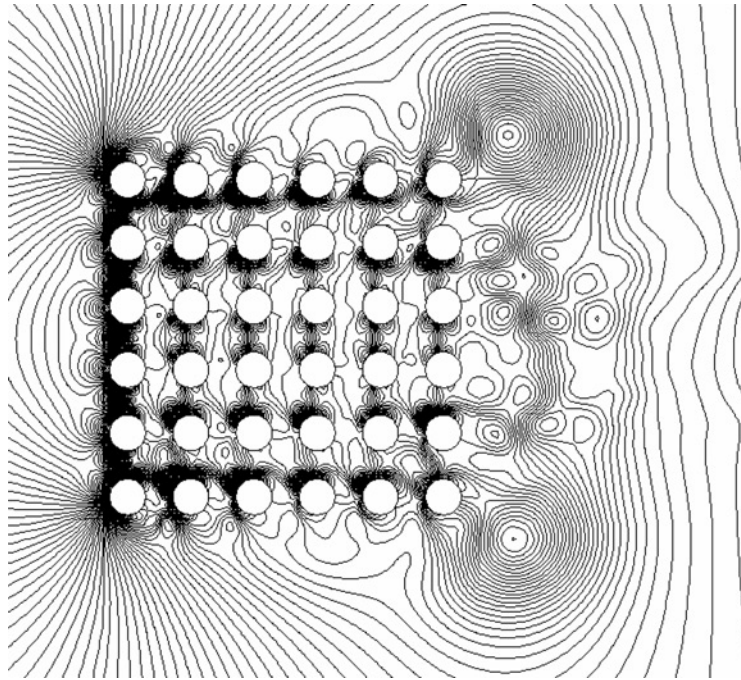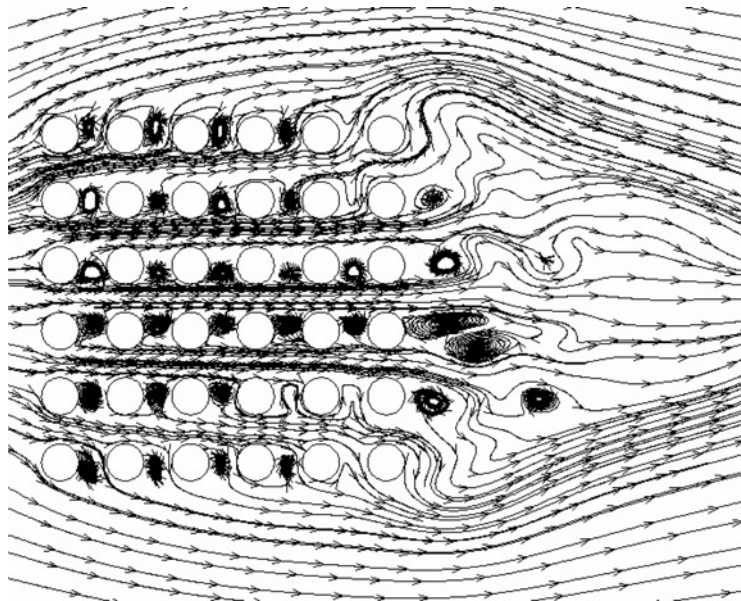cylinders at $tU/D = 20$,
$Re = 100$, and $P/D = 2$

Figure 13.
Streamlines computed for
tube bundle in in-line
square arrangement with
36 cylinders at $tU/D = 20$, $Re = 100$, and
$P/D = 2$

related to the centerline of the tube bundle is completely recognized. Figure 12 shows
that there is high pressure drop (especially after the first column) in the flow through
tube bundle. Low pressure districts behind the bundle are corresponding with the
formed vortices. In the entrance of the bundle, pressure is so high (stagnation points)

therefore the drag is higher for cylinders in the first column related to the others. Figure 13 shows formation of big vortices behind most cylinders of the bundle. The considerable point is that the flow has introduced two different patterns; the pattern of flow through the tube bundle and the pattern of flow around the tube bundle. Here, flow through the tube bundle reached the steady state and has no change with time but the flow around the tube bundle is unsteady and formed vortices behind that travel to the downstream and construct an irregular vortex street.

As a conclusion, based on Figures 11-13, the flow is steady within this arrangement of the tube bundle, but is unsteady behind that. Symmetric flow field for two middle rows led to the zero lift for the cylinders of these rows. Mean value of lift coefficient for all the cylinders of tube bundle is also zero.

As it is presented in Table III, computation of drag coefficients for cylinders shows that maximum drag is 1.06 which belongs to two middle cylinders of the first column. Upper and lower cylinders of these cylinders have a drag coefficient of 0.732. Finally, drag coefficient of most upper and lower cylinders of the first column is 0.551. Drag coefficient decays to 0.2 for second column and very insignificant for the next columns.

The last considerable point is the definition of maximum velocity in the tube bundle called critical velocity. Critical velocity will be used in Connors criteria of tube bundles. For the tube bundle with square or triangular arrangements, based on the analytical approaches, critical velocity is higher than free-stream velocity with the ratio of $P/(P-D)$ (Blevins, 1990). In this manner, critical velocity should be twice the free-stream ($2U$) in the present simulation. While, numerical computation estimated the critical velocity as 0.0043611 and in comparison to the free-stream velocity (0.002505) the ratio will be equal to 1.74. In the meantime, no noticeable higher velocities were observed out of the tube bundle.

5.1.2 Confined case. In this case, the tube bundle in in-line square arrangement is confined by two lateral walls which make more similar configuration to the real situation of the heat exchangers. The gaps between the walls and last rows of the tube bundle are selected equal to the cylinders diameter. The simulation shows that the values of the velocity components, vorticity, and drag coefficients have been increased in comparison with the unconfined case. Maximum drag coefficient have been raised from 1.06 and reached 1.97 while average drag coefficient of tube bundle remained zero due to the symmetric flow pattern (Table III).

Critical velocity reached $2.53U$ and gap velocity between the walls and the last rows of tube bundle is calculated as $2.89U$. Amount of vorticity is reached 1.55 times related to the confined case. Pressure contours and streamlines have had no considerable change with the previous situation.

5.2 Tube bundle in general staggered arrangement
5.2.1 Unconfined case. In this section, unsteady and incompressible viscous flow through an array in a general staggered arrangement is numerically simulated. Figure 14 shows the sketch of tube bundle in the general staggered arrangement, where L is the lateral spacing between adjacent cylinders and T is transverse spacing between adjacent cylinders. The T/D and L/D ratios have been selected as 2 and 1, respectively. 61 circular cylinders are embedded in the bundle. This configuration is frequently used in heat exchangers, nuclear reactors and even porous media. Mesh size and other specification of the simulation are similarly set as the situation of section 5.1.

Consequently, in Figures 15-17, we show snapshot of the vorticity field, pressure contours, and streamlines, respectively, at $tU/D = 20$ and Re $= 100$. Flow through this

Figure 14.
Schematic of flow through
a tube bundle in general
staggered arrangement
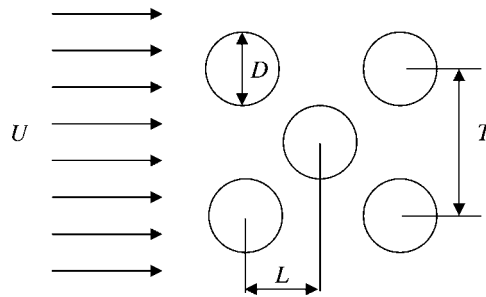
Notes: Figure shows lateral spacing between adjacent cylinders L,
transverse spacing between adjacent cylinders T, tube diameter D
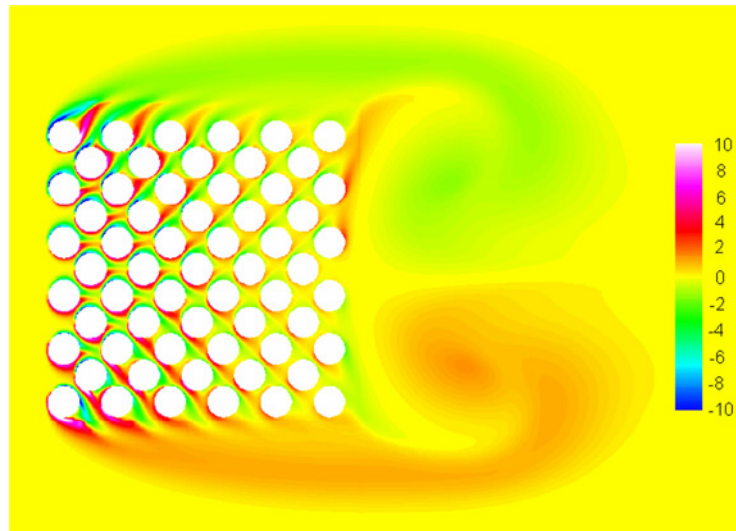and ratios L/D and T/D

Figure 15.
Vorticity field computed
for tube bundle in general
staggered arrangement
with 61 cylinders at $tU/D = 20$, Re $= 100$, $T/D = 2$, and $L/D = 1$

arrangement is also steady like previous arrangement. The reason is the vicinity of
embedded cylinders and their little spacing that avoided vortex shedding behind every
cylinder. From Figure 15 is observed that there is no symmetry in axes of every
cylinder (except five cylinders on the centerline of the tube bundle), therefore lift forces
are produced, in contrary with the previous arrangement. But mean lift coefficient is
zero in the tube bundle due to the existence of general symmetry axes. Here, the flow
around the tube bundle implies the flow around bluff bodies by rectangular cross
sections. Two big vortices are symmetrically formed behind the tube bundle. Pressure
distribution (Figure 16) shows that the flow has not extremely penetrated into the tube
bundle. The reason is that the tube bundle were not confined by lateral walls, otherwise
the flow would have been forced to pass through the cylinders. And also the high
pressure regions are not limited to the first column of the bundle but the region is like a
triangle where first column is its base and its head is the center point of the bundle.
This led to the fact that drag coefficient was not significantly different in the first
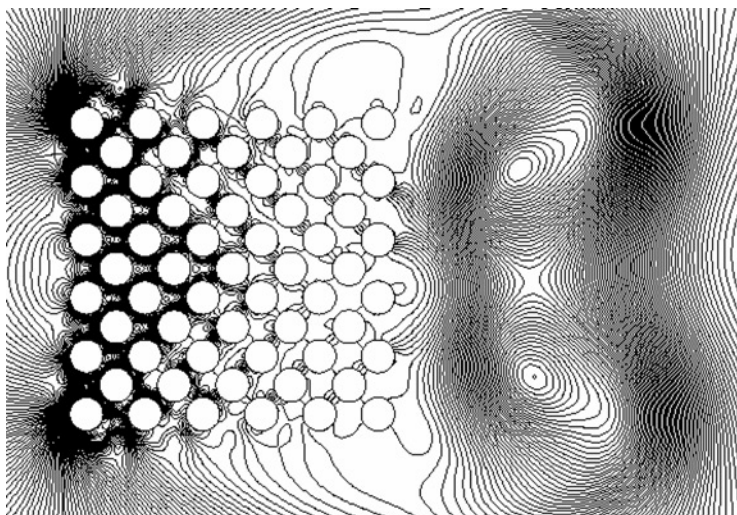column. Low pressure regions which are the place of two big vortices are recognized

behind the bundle. The streamlines in Figure 17 exhibit extremely tortuous paths of flows through the tubes. Also, there is no vortex behind the cylinders due to the low spacing of them.

Computation of drag coefficients for cylinders shows that maximum drag is 0.751 which belongs to the first cylinder from upper-left side and its opposite cylinder in lower-left side. Drag coefficient in the second column which consists of staggered cylinders, is negligible and mean drag coefficient in the third column is calculated as 0.209. Furthermore, drag coefficients are negligible for the next columns. Therefore, supporting the first and the third column in heat exchangers with general staggered tube bundle is more important.

Numerical computation estimated the critical velocity as 0.0046838. Regarding the amount of free-stream velocity (0.002505) the ratio will be equal to 1.87, while there are

higher velocities out of the tube bundle with the ratio of 1.96 related to the free-stream velocity. On the other hands, this tubes arrangement guides the flow around the bundle with higher velocity.

5.2.2 Confined case. In this case the values of the velocity components, vorticity, and drag coefficients have been significantly raised. Maximum drag and lift coefficients are increased from 0.75 to 2.75 and from 0.46 to 0.74, respectively (Table III). Clearly, drag coefficient has had considerable growth.

Critical velocity reached $2.49U$ and gap velocity between the walls and the last rows of tube bundle is calculated as $5.84U$. Amount of vorticity is reached 3.07 times related to the confined case of this configuration.

Streamlines pattern has completely changed and the big vortices are not appeared stationary behind the bundle. Here, small vortices formed and travel to the down stream of flow field.

6. Conclusion

A finite-volume based Cartesian-staggered grid method has been implemented which allows us to simulate unsteady, viscous flows tube bundles. A simple procedure has been implemented which allows the selection of ghost-cells for applying the no-slip condition. No-slip condition has been enforced using a linear interpolation on the ghost-cells' preserves of the second order accuracy of the discretization. The grid was finer in the region of the bluff bodies.

Cavity flow has been solved for calibration of the solver and verification of the results in a case which no boundary are embedded in the domain. Then the simulations of flow past a circular cylinder subjected to a uniform free-stream have also been carried out in the Reynolds number range 10-300. Key quantities such as the mean drag coefficient, vorticity field, and vortex shedding Strouhal number obtained from our simulations agree well with the established experimental and numerical results. It is concluded that in the absence of three-dimensionality, the solver has a reasonable accuracy.

In order to analyze the flow through tube bundles, we have simulated two relatively complex flows; the flow through in-line square and general staggered arrangements with 36 and 61 cylinders, respectively. Results were in good agreement with the literature and show that the maximum drag is 1.06 which belongs to two middle cylinders of the first column in square arrangement. While the maximum drag coefficient in the general staggered arrangement is 0.751 which belongs to the first cylinder from up and left side and its opposite cylinder in down and left side. Therefore, drag coefficient is highest in the first column of these arrangements. For the cases where tube bundles are confined, maximum drag coefficients reached 1.97 and 2.75, respectively.

Two different flow patterns have been observed in both arrangements; the pattern through the bundles and the pattern around the bundles. Internal pattern is steady and has no change with time. External pattern for square arrangement is unsteady with irregular vortex shedding. While, external pattern of general staggered arrangement consist twin fixed vortices formed behind the bundle.

The ratio of the critical velocity to the free-stream velocity for in-line square tube bundle and general staggered tube bundle is equal to 1.74 and 1.87 which can be directly used in the calculation of Connors criteria. Values of 2.53 and 2.49 are obtained for confined cases, respectively.

Eventually, as a marginal conclusion, we find that the current method has no difficulty in resolving the complex flow pattern through tube bundles. It can be a

powerful tool to study fluid-structure interaction. The authors plan to simulate flows at high Reynolds numbers in order to predict fluid-elastic instability in tube bundles which will be presented in an individual article.

References

Almgren, A.S., Bell, J.B., Colella, P. and Marthaler, T. (1997), "A Cartesian grid projection method for the incompressible Euler equations in complex geometries", *SIAM Journal on Scientific Computing*, Vol. 18 No. 5, p. 1289.

Bayyuk, S.A., Powell, K.G. and Van Leer, B. (1993), "A simulation technique for 2-D unsteady inviscid flows around arbitrarily moving and deforming bodies of arbitrary geometry", AIAA Paper, 93-3391-CP.

Blevins, R.D. (1990), *Flow-Induced Vibration*, Van Nostrand Reinhold, New York, NY.

Dennis, S.C.R. and Chang, G. (1970), "Numerical solutions for steady flow past a circular cylinder at Reynolds numbers up to 100", *Journal of Fluid Mechanics*, Vol. 42, pp. 471-89.

Ghia, U., Ghia, K.N. and Shin, C.T. (1982), "High-resolutions for incompressible flow using the Navier–Stokes equations and a multigrid method", *Journal of Computational Physics*, Vol. 48, pp. 387-411.

Henderson, R.D. (1995), "Details of the drag curve near the onset of vortex shedding", *Physics of Fluids*, Vol. 7, pp. 2102-4.

Hou, S. and Zou, Q. (1995), "Simulation of cavity flow by the lattice Boltzmann method", *Journal of Computational Physics*, Vol. 118, pp. 329-47.

Kevlahan, N.K., and Wadsley, J. (2005), "Suppression of three-dimensional flow instabilities in tube bundles", *Journal of Fluids and Structures*, Vol. 20, pp. 611-20.

Kravchenko, A.G., Moin, P. and Shariff, K. (1999), "B-Spline method and zonal grids for simulations of complex turbulent flows", *Journal of Computational Physics*, Vol. 151, pp. 757-89.

Lima E. Silva, A.L.F., Silveira-Neto, A. and Damasceno, J.J.R. (2003), "Numerical simulation of two-dimensional flows over a circular cylinder using the immersed boundary method", *Journal of Computational Physics*, Vol. 189, pp. 351-70.

Liu, Q. and Vasilyev, O.V. (2007), "A Brinkman penalization method for compressible flows in complex geometries", *Journal of Computational Physics.*, Vol. 227, pp. 946-66.

Longatte, E., Bendjeddou, Z. and Souli, M. (2003), "Methods for numerical study of tube bundle vibrations in cross-flows", *Journal of Fluids and Structures*, Vol. 18, pp. 513-28.

Park, J., Kwon, K. and Choi, H. (1998), "Numerical solutions of flow past a circular cylinder at Reynolds number up to 160", *KSME International Journal*, Vol. 12, p. 1200.

Patankar, S.V. (1980), *Numerical Heat Transfer and Fluid Flow*, Hemisphere Publishing, New York, NY.

Patankar, S.V. and Spalding, D.B. (1972), "A calculation procedure for heat, mass and momentum transfer in tree-dimensional parabolic flows", *International Journal of Heat Mass Transfer*, Vol. 15, p. 1787.

Pember, R.B., Bell, J.B., Colella, P., Crutchfield, W.Y. and Welcome, M.L. (1995), "An adaptive Cartesian grid method for unsteady compressible flow in irregular regions", *Journal of Computational Physics*, Vol. 120, p. 278.

Quirk, J.J. (1994), "An alternative to unstructured grids for computing gas dynamic flows around arbitrarily complex two-dimensional bodies", *Computers & Fluids*, Vol. 23 No. 1, p. 125.

Roshko, A. (1955), "On the wake and drag of bluff bodies", *Journal of the Aeronautical Sciences*, Vol. 22, p. 124.

Schneider, K. and Farge, M. (2005), "Numerical simulation of the transient flow behavior in tube bundles using a volume penalization method", *Journal of Fluids and Structures*, Vol. 20, pp. 555-66.

Schroder, K. and Gelbe, H. (1999), "New design recommendations for fluid-elastic instability in heat exchanger tube bundles", *Journal of Fluids and Structures*, Vol. 13, pp. 361-79.

Shyy, W., Udaykumar, H.S., Rao, M.M. and Smith, R.W. (1996), *Computational Fluid Dynamics with Moving Boundaries*, Taylor and Francis, London.

Sweeney, C. and Meskell, C. (2003), "Fast numerical simulation of vortex shedding in tube arrays using a discrete vortex method", *Journal of Fluids and Structures*, Vol. 18, pp. 501-12.

Tritton, D.J. (1959), "Experiments on the flow past a circular cylinder at low Reynolds numbers", *Journal of Fluid Mechanics*, Vol. 6, pp. 547-67.

Tseng, Y.H. and Ferziger, J.H. (2003), "A ghost-cell immersed boundary method for flow in complex geometry", *Journal of Computational Physics*, Vol. 192, pp. 593-623.

Udaykumar, H.S., Shyy, W. and Rao, M.M. (1996), "ELAFINT: A mixed Eulerian–Lagrangian method for fluid flows with complex and moving boundaries", *International Journal for Numerical Methods in Fluids*, Vol. 22, p. 691.

Udaykumar, H.S., Kan, H.C., Shyy, W. and Tan-Son-Tay, R. (1997), "Multiphase dynamics in arbitrary geometries on fixed Cartesian grids", *Journal of Computational Physics*, Vol. 137, p. 366.

Williamson, C.H.K. (1996), "Vortex dynamics in the cylinder wake", *Annual Review of Fluid Mechanics*, Vol. 28, pp. 477-539.

Ye, T., Mittal, R., Udaykumar, H.S. and Shyy, W. (1999), "An accurate Cartesian grid method for viscous incompressible flows with complex immersed boundaries", *Journal of Computational Physics*, Vol. 156, pp. 209-40.

Zdravistch, F., Fletcher, C.A. and Behnia, M. (1995), "Numerical laminar and turbulent fluid flow and heat transfer predictions in tube banks", *International Journal of Numerical Methods for Heat and Fluid Flow*, Vol. 5 No. 8, pp. 717-33.

Further reading

Grove, A.S., Shair, F.H., Petersen, E.E. and Acrivos, A. (1964), "An experimental investigation of the steady separated flow past a circular cylinder", *Journal of Fluid Mechanics*, Vol. 19, pp. 60-80.

Lai, M.C. and Peskin, C.S. (2000), "An immersed boundary method with formal second-order accuracy and reduced numerical viscosity", *Journal of Computational Physics*, Vol. 160, p. 705.

Thom, A. (1933), "Numerical solution for the flow around a cylinder at Reynolds numbers of 40, 200 and 500", *Proceedings of the Royal Society A*, Vol. 141, pp. 651-69.

Corresponding author
Hamed Houri Jafari can be contacted at: hhjafari@modares.ac.ir